Available online at www.sciencedirect.com
ScienceDirect
Acta Materialia 58 (2010) 1016–1025
Acta MATERIALIA
www.elsevier.com/locate/actamat

Au–Fe alloy solidification and solid-state transformations

D. Favez *, J.-D. Wagnière, M. Rappaz

Laboratoire de Simulation des Matériaux, École Polytechnique Fédérale de Lausanne, Station 12, CH – 1015 Lausanne, Switzerland

Received 21 July 2009; received in revised form 30 September 2009; accepted 11 October 2009
Available online 14 November 2009

Abstract

In order to better understand the microstructure that forms during laser welding of an 18 carat gold and an austenitic stainless steel, solidification of the Au–Fe binary analog has been studied using thermal analysis and interrupted Bridgman experiments. For a hypoperitectic composition, the formation of the primary phase, its coarsening and the peculiar macrosegregation associated with the large density difference between the elements have been studied. Just after the peritectic phase forms around the primary dendrites, continuous and discontinuous precipitation has been shown to occur as a result of the immiscibility of the two face-centered cubic phases below the peritectic temperature. Finally, the solid-state transformations associated with the eutectoid have been characterized.

Keywords: Au–Fe; Differential thermal analysis (DTA); Peritectic solidification; Discontinuous precipitation; Coherency relationship

1. Introduction

In jewelry manufacturing, joining dissimilar materials is usually achieved by brazing. However, since this technique has several disadvantages [1,2], including undesired phase transformations and softening of the base materials during heat treatment, alternative joining methods such as laser welding are now being considered. Thanks to its high energy density and precise delivery using, for example, optical fibers, a laser beam can locally melt well-defined amounts of the base alloys located near the interface, without affecting the bulk microstructure of the parts to be joined [3]. However, this method produces an entirely new alloy in the weld trace and thus requires a thorough understanding of the microstructure that forms during solidification.

When the two alloys to be joined are multicomponent, the analysis can become quite difficult. As a first approximation, it might be useful to consider the binary system made out of the main elements constituting the base alloys to be welded. In the present study, the welding metallurgy of an austenitic stainless steel and a classical 18 carat yellow gold (Au–12.5 wt.% Ag–12.5 wt.% Cu) has been approximated by the solidification analysis of the Au–Fe system. In this binary alloy, the primary solid phase that solidifies for a Au composition between 11 and 43 at.% is austenite (γ-Fe), as can be seen on the phase diagram shown in Fig. 1. On the other side of the phase diagram, pure Au is an approximation of the Au–Ag–Cu solid solution of the 18 carat yellow gold.

Except for the establishment of the phase diagram [4–6], very few studies have been conducted on the solidification and high-temperature precipitation in the Au–Fe system. To the present authors' knowledge, all recent studies on this system have been focused on the precipitation of Fe from supersaturated face-centered cubic (fcc) Au–Fe solid solution, for compositions higher than 60 at.% Au and at temperatures lower than 600 °C. Indeed, such alloys have been shown to present interesting magnetic properties, including the giant magnetoresistive effect (GMR) [7,8].

At higher temperature, solidification of the primary phase and the peritectic reaction (γ-Fe) + liquid ↔ (Au) at 1173 °C are of primary importance for alloys containing 8–43 at.% gold, as will be shown in the present contribution. The peritectic invariant is in fact characterized by two solid phases, (γ-Fe) and (Au), which have the same fcc structure and exhibit a miscibility gap for temperatures lower than 1248 °C. Because of the existence of high-temperature equilibrium

* Corresponding author.
E-mail addresses: denis.favez@a3.epfl.ch (D. Favez), jean-daniel.wagniere@epfl.ch (J.-D. Wagnière), michel.rappaz@epfl.ch (M. Rappaz).

1359-6454/$36.00
doi:10.1016/j.actamat.2009.10.017

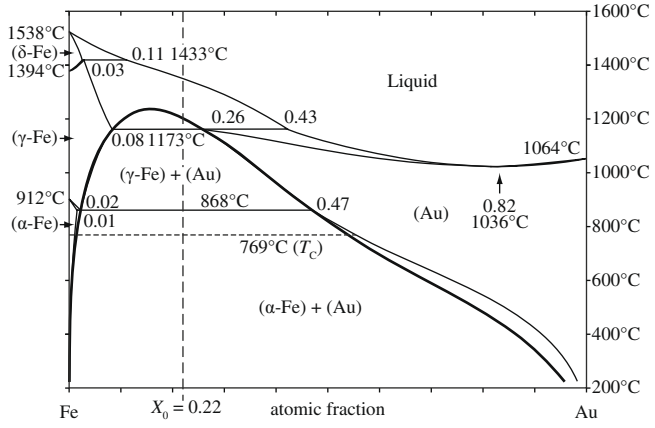

Fig. 1. Au–Fe phase diagram redrawn from Ref. [4]. The thick line represents the metastable miscibility gap of the fcc phase, calculated with the common tangent method with data from Ref. [4].

between this fcc phase and the liquid, what could have been a spinodal decomposition (see the thick line in Fig. 1) is then a peritectic reaction. This miscibility gap appears as a two-phase region with strong solvus retrogrades between the peritectic temperature and the temperature of 868 °C at which the eutectoid transformation (γ-Fe) $\leftrightarrow$ (Au) + (α-Fe) occurs. As will be shown, these retrogrades play an important role in solid-state transformations since the solubility of each element in the other phase decreases with temperature, thus inducing a continuous driving force for precipitation of (γ-Fe) from the (Au) matrix, and of (Au) from the (γ-Fe) matrix.

Below the eutectoid temperature, the solubilities of Fe in Au and of Au in Fe keep decreasing, leading to discontinuous precipitation of (α-Fe) [9–12]. According to Bosco [13], there is actually a competition between precipitation of (α-Fe) and (γ-Fe) in the (Au) matrix. The body-centered cubic (bcc) phase is stable, whereas the fcc form is metastable, but requires a lower driving force for nucleation (as the matrix is also fcc). Furthermore, the compositions of stable (α-Fe) and metastable (γ-Fe) are close to each other, as can be seen in Fig. 1. Therefore, phase selection is strongly related to defect concentration.

The aim of this study is to observe and understand the formation and evolution of microstructure during solidification and solid-state transformations of a hypoperitectic Au–Fe alloy. Differential thermal analysis (DTA) and directional solidification in a Bridgman-type furnace (DSB) have been carried out. Specimens quenched during DSB were then characterized using electron microscopy. Solidification of the primary phase, the peritectic reaction and subsequent solid-state transformations were investigated.

2. Experimental methods

2.1. Thermal analysis

Thermal analysis was conducted on a Boersma DTA, also known as heat-flux DSC (Netzsch DSC 404C Pegasus). In such a device, the sample and the reference are contained in small alumina crucibles placed over bases. Thermocouples are attached to the bases and the whole setup is placed within the same furnace, i.e. identical thermal conditions [14]. An enthalpy change associated with a phase transformation in the sample induces a small temperature difference compared to the reference. This difference can be recorded and converted into enthalpy using a suitable calibration. In the present case, the reference was an empty crucible and the Au–Fe sample weighed typically 20 mg. It was prepared by simply placing Au and Fe (99.99% purity) in the right proportion into the DTA crucible. Providing these two elements were in close contact, a first melting ensured perfect mixing of the metals by surface tension forces (Marangoni solutal convection). DTA measurements upon heating and cooling were then performed at the same rate ($\pm$10 K min^{-1}).

2.2. Interrupted Bridgman solidification

Directional solidification experiments of Au–Fe specimens were undertaken for a hypoperitectic composition of 22 at.% Au (dashed line in Fig. 1), i.e. about 50 wt.% Au. This was achieved using a high thermal gradient, vertical Bridgman furnace [15], which consisted of two parts: a hollow molybdenum susceptor heated by an induction coil and placed in a protective atmosphere for the heating stage, and a water-cooled liquid metal (LMC) bath for the cooling stage.

Taking advantage of the large density difference between Au and Fe, the specimens were prepared as follows in order to ensure a homogeneous initial composition of the sample. Fe powder (99.99% purity) was placed at the bottom of an alumina tube of 4 mm inner diameter, with the gold pellets (99.99% purity) placed above. At the beginning of the experiment, the specimen was lowered into the cold zone of the furnace. After the temperature of the furnace was raised and stabilized at 1500 °C, the crucible was slowly pulled up at 2 mm s^{-1}, allowing gold pellets to melt first. The liquid gold then seeped into, and dissolved, the iron powder. When the whole sample was liquid, the crucible was pulled down at the selected velocity (33.4 or 1.67 μm s^{-1}, which correspond to cooling rates of 0.66 and 0.034 K s^{-1}, respectively). After a certain length of solidification, the crucible was dropped suddenly into the LMC bath. This rapid quench froze the remaining liquid with a very fine microstructure, which was clearly distinct from that growing under steady-state conditions, thus allowing the latter to be observed at room temperature. The average thermal gradient measured in the mushy zone with an inserted thermocouple was around 300 K cm^{-1} (the value close to the liquidus being slightly lower, 280 K cm^{-1}) [16].

2.3. SEM-BSE image analysis of Bridgman sample

After quenching, the samples were sectioned along the longitudinal axis and hot mounted in a conductive resin

for electron microscopy observations. In scanning electron microscopy (SEM), the number of electrons backscattered by a specimen is directly related to the atomic number of the atoms under the beam. Therefore, backscattered electron (BSE) analysis provides direct information on the chemical composition. For binary systems, the BSE intensity can even be used as a semiquantitative analysis tool, especially when the elements involved have a drastically different atomic number such as in the Au–Fe system (79 and 26, respectively).

The backscattering coefficient η_i of an element i is the probability that an incident electron will be backscattered. This coefficient can be expressed as a third-order polynomial of the atomic number Z_i. In a homogeneous mixture, the average BSE coefficient is related to the weight fraction C_i of the components by a simple rule of mixture [17]:

$$\eta_{mix} = \sum_i C_i \eta(Z_i) \tag{1}$$

As the BSE intensity I is proportional to the number of backscattered electrons $n = \eta_{mix} I_0$, where I_0 is the flux of incident electrons, two parameters A and B related to brightness and contrast can be defined:

$$I = An + B \tag{2}$$

Therefore, with proper calibration, the BSE intensity can be directly converted into composition. This simple method also allows easy measurement of the volume fraction of a phase from a single BSE image, providing each phase has a sufficiently distinct composition. Indeed, a phase described by a composition range can be converted into a range of gray-levels. Providing this range does not overlap with that of another phase, the pixel intensity distribution gives direct information on the distribution of the phases.

3. Thermal analysis results

DTA curves measured upon cooling and heating an Fe–22 at.% Au specimen are shown in Fig. 2. As the temperature of the apparatus was measured during heating, transition temperatures deduced from the curves measured during cooling must be considered as semiquantitative.

The first peak appearing on the cooling curve corresponds to the solidification of the primary (γ-Fe) phase (liquidus temperature $T_{liq} = 1360\,^{\circ}C$). Due to the small mass and the high purity of the specimen, few heterogeneous nucleation sites are available. Consequently, a significant undercooling of 80 K is measured for the first solid appearance. Following nucleation, the fast growth of austenite dendrites at this high undercooling releases a large amount of latent heat. This induces a very rapid temperature increase of the specimen (recalescence) and a narrow, off-scale DTA peak labeled 1 in Fig. 2. Following this recalescence, the release of latent heat associated with the growth and thickening of the (γ-Fe) dendrites is greatly reduced, but can nevertheless still be observed from the deviation of the measured DTA curve from the baseline (dashed line).

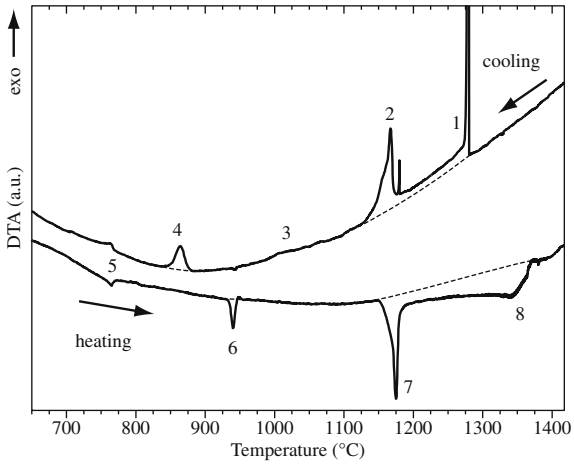

Fig. 2. DTA curves of an Fe–22 at.% Au specimen upon heating and cooling at ± 10 K min^{-1}. See text for legend.

Peak # 2 is associated with the peritectic invariant, i.e. the appearance of the (Au) phase at $T_{per} = 1173\,^{\circ}C$ (see Fig. 1). However, the fact that it is made of two peaks, a sharp one at 1180 °C and a broader one starting at 1173 °C, is puzzling. Double nucleation peaks below T_{per} have been reported in the literature, but were finally related to the initial nucleation of the primary phase below the peritectic temperature, followed by the nucleation of the peritectic phase [18]. In the present study, the solidification peak of the primary phase is clearly visible and distinct from peak # 2, so that this mechanism can safely be discarded. Furthermore, it has been observed at high cooling rates that nucleation of the peritectic phase can occur above T_{per} [19]. This can occur when the undercooling of the primary phase is large enough to allow formation of the peritectic phase in a highly undercooled liquid. This mechanism can also be eliminated for two reasons: first, the cooling rate is very low, and second, this would not result in a second peak on the DTA curve. A third mechanism could be the formation of a metastable peritectic phase instead of the stable one, e.g. Al_9Ti instead of Al_3Ti in the Al–Ti system. However, this mechanism is unlikely in the Au–Fe system.

Another explanation for the nucleation of the peritectic phase above T_{per} is as follows. Unlike the formation of (γ-Fe) with a large undercooling (peak # 1), heterogeneous nucleation of (Au) is much easier due to the presence of the austenite dendrites having the same crystallographic structure. This event can even occur at higher temperature than T_{per} if $\gamma_{Fe\ell} > \gamma_{FeAu} + \gamma_{Au\ell}$, where $\gamma_{Fe\ell}$, $\gamma_{Au\ell}$ and γ_{FeAu} are the interfacial energies between (γ-Fe) and liquid, (Au) and liquid and (γ-Fe) and (Au), respectively. Although these values are unknown, this event is probable if one considers that the interfacial energy of molten iron with air (or vacuum) is about twice that of molten gold [20]. This could explain why the first sharp peak # 2 is slightly above the equilibrium peritectic temperature, but not why it is separate from the second, broader one.

Finally, it should be remembered here that the temperature of the apparatus was calibrated for heating: this negative undercooling may also be within the error of the measurement. Furthermore, the separate peak cannot be related to the nucleation event alone and the broader peak to the growth of the (Au) phase: the growth starts immediately after nucleation, and both events should appear in the same peak. No rational explanation has been found for this separate peak.

Once nucleated, the (Au) phase solidifies according to microsegregation, i.e. to diffusion in the peritectic phase. Because the thickness of this phase is fairly small and diffusion in (Au) is substantially faster than in (γ-Fe) [21], (Au) solidifies with very little microsegregation. It will then end approximately at the solidus of the composition of the liquid once (Au) formed (i.e. $C_\ell = 43$ at.% at T_{per}, Fig. 1). The solidification interval associated with this composition (about 50 K) compares well with the width of the broad peak # 2.

Between 1100 and 1050 °C, the DTA curve shows small exothermic deviations (# 3), that may be related to the precipitation of (γ-Fe) in the peritectic (Au) phase, and of (Au) in (γ-Fe), due to the decreasing solubilities of iron in (Au), and of gold in (γ-Fe). At 875 °C, peak # 4 is indicative of the eutectoid transformation, where (γ-Fe) is transformed into (α-Fe) and (Au) ($T_{eut} = 868$ °C, see Fig. 1). Peak # 5 at 760 °C corresponds to the Curie temperature, i.e. transition from paramagnetic to ferromagnetic state on cooling.

Focusing now our attention on the DTA curve upon heating, the endothermic peak # 6 at 932 °C (after the reverse magnetic transition, peak # 5) corresponds to the transformation of ferrite (α-Fe) into austenite (γ-Fe). According to the phase diagram, this transformation should occur between $T_{eut} = 868$ °C and the allotropic transformation temperature of pure iron at 912 °C. However, the kinetics of this transformation is dictated by nucleation and diffusion, i.e. by the formation and growth of (γ-Fe) nuclei. Peak # 7 between 1150 and 1173 °C corresponds to the melting of the (Au) phase. If equilibrium is assumed, i.e. lever rule at any instant, melting of the peritectic phase should occur at T_{per}. However, due to limited diffusion, especially in the solid state, melting starts at the solidus of the Au-rich zones and ends at T_{per}. It appears that peak # 7 is less spread (and single) than its counterpart peak # 2, indicating that some homogenization has occurred during the cooling–heating cycle. Above this peak, the (γ-Fe) phase gradually melts (deviation from the base line) up to the liquidus of the alloy. This temperature (1360 °C), corresponding to the end of the latent heat absorption, coincides fairly precisely to the beginning of the temperature increase (peak # 8), before the DTA curve returns to the baseline.

4. Interrupted Bridgman solidification results

4.1. Global SEM analysis

The microstructure formed in an Fe–22 at.% Au alloy solidified in the Bridgman furnace at 1.67 μm s^{-1} and then quenched in the LMC bath is shown in Fig. 3. This is a longitudinal section observed in SEM-BSE, i.e. the dark/light contrast corresponds to Au-lean/rich zones. The thermal gradient is toward the left with a temperature scale at the bottom of the figure deduced from the thermocouple reading. The various phase transformations that can be observed in this section are enlarged in the five zooms at the top: the primary (γ-Fe) solidification (a), the peritectic phase formation (b), the decomposition of the fcc phase in the miscibility gap (precipitation of (Au) into (γ-Fe) and of (γ-Fe) into (Au)) (c), the eutectoid reaction (d), and finally the precipitation of (α-Fe) within the (Au) phase. These are detailed below.

Fig. 4 presents the phase distribution obtained from the analysis of the gray-levels of SEM-BSE images taken at 14 positions on Fig. 3 and corresponding to temperatures ranging from 1300 to 480 °C. At a given temperature, i.e. height in the quenched specimen, each peak in the gray-level intensity distribution can be attributed to a phase, its area to the volumetric fraction, its position to the mean composition and its width to the composition variations within the phase. The evolution of the peak with temperature is therefore an indication of the phase composition and volumetric fraction variations.

At 1300 °C, two phases can be seen: liquid and primary (γ-Fe). The austenite composition is very well defined, whereas that of the liquid exhibits a broader peak due to the quench which produces a fine microstructure with composition variations. The peritectic invariant at T_{per} is clearly revealed by this gray-level analysis, as a new peak of intermediate composition can be seen to appear at the expense of the liquid peak, which disappears. Below this temperature and down to about 1000 °C, the peritectic (Au) and primary (γ-Fe) phases get richer in their respective elements as a result of the solvus retrogrades of the phase diagram (see Fig. 1). As will be seen, this corresponds to regions near the (Au)–(γ-Fe) interface for which no precipitation is needed to follow the solvus lines (short diffusion path, particle-free zone). The (γ-Fe) peak suddenly shifts to lower X_{Au} while the (Au) peak shifts to higher X_{Au}—evidence of (Au) precipitation in the (γ-Fe) phase and of (γ-Fe) precipitation in the (Au) phase. The eutectoid reaction is indicated by a second abrupt shift of the low-X_{Au} peak around 870 °C corresponding to the iron phase, since gold is less soluble in (α-Fe) than in (γ-Fe). Finally, it can be seen that the composition of the (Au) phase continuously increases from its formation at T_{per} down to about 500 °C, at which point the atomic mobility is too low and the microstructure becomes frozen.

The similarities between Fig. 4 and the Au–Fe phase diagram (Fig. 1) are striking: the peak maxima correspond to the liquidus, solidus and solvus lines. Invariants such as the peritectic at 1173 °C are seen as the coexistence of three peaks, which is thermodynamically equivalent to the coexistence of three phases with equal chemical potentials. However, a few differences remain: first, the kinetics of nucleation and growth are reflected in Fig. 4, thus shifting

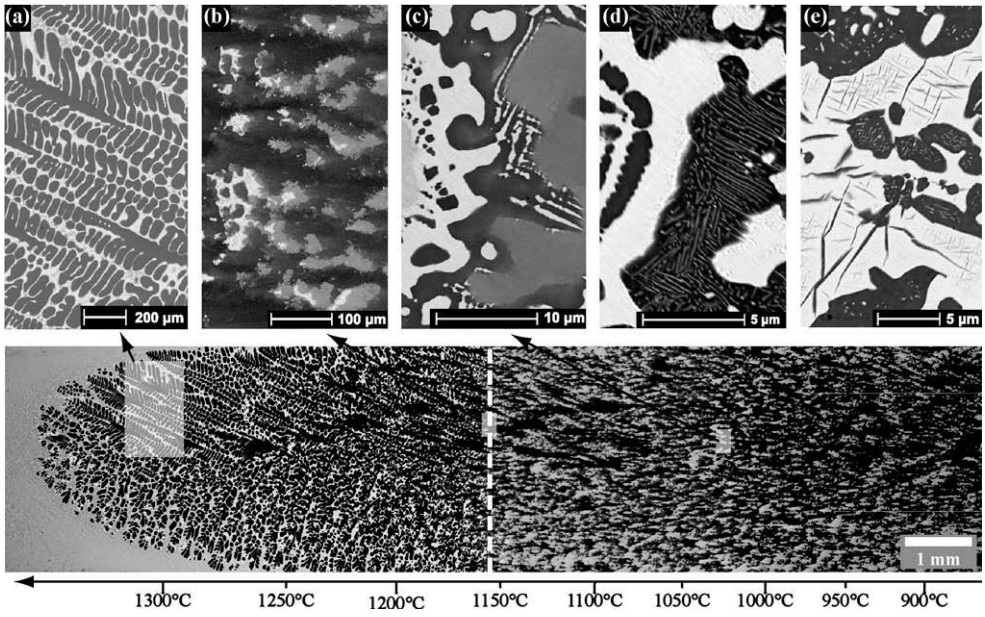

Fig. 3. Solidification microstructure of an Fe–22 at.% Au alloy solidified in a Bridgman furnace at 1.67 μm s^{-1}, longitudinal section, backscattered electrons. The thermal gradient is oriented toward the left. (a) Primary phase (γ-Fe) solidification; (b) peritectic phase formation; (c) decomposition of the fcc phase; (d) eutectoid reaction; (e) (α-Fe) ferrite precipitation in (Au).

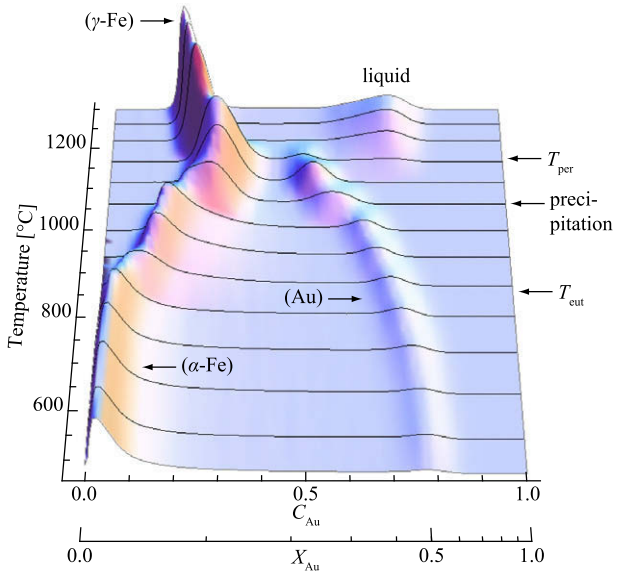

Fig. 4. SEM-BSE image analysis of Fig. 3, showing the evolution of the composition and volumetric fraction of phases. The first scale in wt.% (C_{Au}) obtained from the measurement has been converted into at.% (X_{Au}).

the transition temperatures to lower values; second, if the transformation kinetics is too fast, it does not appear in Fig. 4. This is the case, for example, of the fairly rapid solidification of the peritectic phase, which does not allow observation of the beginning of the (Au)–liquid two-phase region.

4.2. Solidification

As can be seen in Fig. 3, the solidification of the primary phase is clearly dendritic, even at this low growth rate ($v = 1.67$ μm s^{-1}) in a high thermal gradient ($G = 3\times 10^4$ K m^{-1}). This is expected since the characteristic thermal distance given by $\Delta T_0/G \approx 5$ mm, where ΔT_0 is the solidification interval of the (γ-Fe) phase, is still larger than the solute boundary layer of a planar front, $D_\ell/v \approx 2$ mm, where D_ℓ is the diffusion coefficient in the liquid. Furthermore, the dendritic front has a highly convex shape as a result of macrosegregation. During solidification of (γ-Fe), gold is segregated into the liquid phase, thus increasing its density. In the Bridgman furnace with G oriented toward the top, i.e. opposite to gravity, the situation is therefore stagnant from both thermal and solutal points of view. However, in the presence of a small radial component of the thermal gradient, the isotherm of the liquidus temperature is slightly convex [16]. In such a situation, the Au-rich liquid has a tendency to move toward the periphery of the specimen, which then induces a positive segregation near the surface of the crucible and a negative one at the center of the specimen. This increases the curvature of the dendritic front, compared to that of the isotherms, leading to the highly convex shape seen in Fig. 3 [22].

The orientation of the dendrite trunks in Fig. 3a is the same, indicating that they belong to the same grain. The in-plane angle of these trunks to the thermal gradient is 24°. On the other hand, their out-of-plane angle can be estimated from their extension in the metallographic section, assuming that they are cylindrical in three dimensions. Their length/width ratio gives an out-of-plane angle of about 7°. Since dendrites in cubic phases grow along ⟨1 0 0⟩ directions [23], this gives two of the Euler angles characterizing the ⟨1 0 0⟩ axes with respect to the specimen coordinate system. The third Euler angle could normally be deduced from the appearance of the secondary arms. However, the arms in Fig. 3a are not exactly perpendicular to

the trunks and are tilted in the direction of G. This observation can be related to the solidification conditions: at the high G/v ratio, growth is not very far from the cellular regime and secondary arms are influenced by the thermal conditions, making them to deviate from the usual $\langle 100 \rangle$ directions. Nevertheless, these arms are mostly in the plane of the section, indicating that the third angle is small.

Coarsening of these secondary dendrite arms is shown in Fig. 5, where their spacing λ_2 is plotted as a function of the local solidification time t, using logarithmic scales. Compared to the standard coarsening law $\lambda_2 \propto t^{1/3}$ [23], a least-squares fit of these data gives $\lambda_2 \propto t^{1/3.55}$. This reduced exponent can be attributed to the diffusion coefficient D_ℓ which decreases with temperature, and thus over time.

4.3. Peritectic phase formation

Around 1173 °C, the peritectic phase (Au) forms as shown in more detail in Fig. 6. According to Ref. [18], three phenomena have to be considered: the peritectic reaction near the triple junction, the peritectic solidification, and the peritectic transformation.

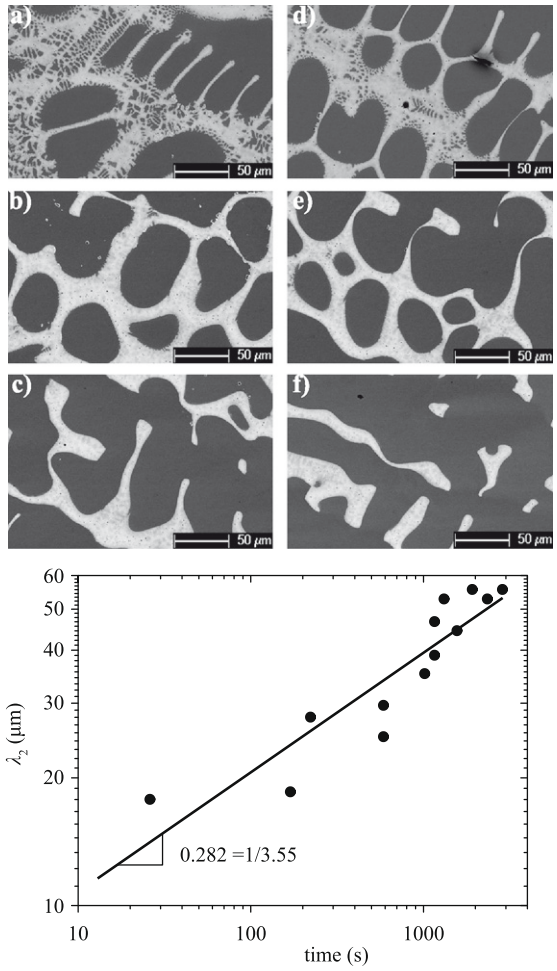

Fig. 5. Top: closer look at the coarsening of secondary dendrite arms show in Fig. 3. (a) 20 s, 1340 °C; (b) 980 s, 1307 °C; (c) 1600 s, 1286 °C; (d) 2000 s, 1272 °C; (e) 2350 s, 1260 °C; (f) 2900 s, 1240 °C. Down: log–log plot of λ_2 as a function of time. $\lambda_2 \propto t^{1/3.55}$ is a least-squares fit.

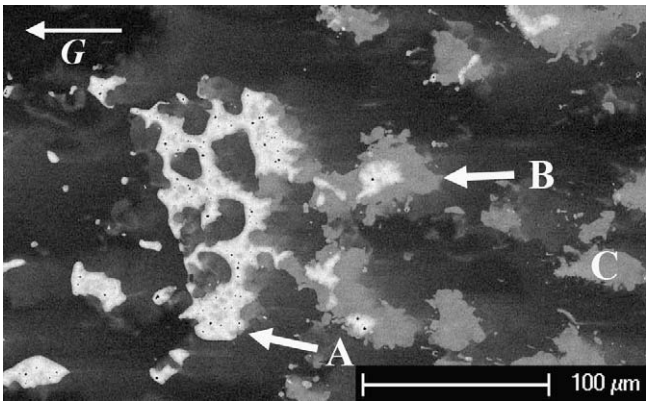

Fig. 6. Peritectic phase formation: (A) peritectic reaction; (B) solid-state peritectic transformation; (C) end of peritectic phase solidification. The thermal gradient G is oriented toward the left.

It is difficult to discern in this microstructure whether the formation of the peritectic phase between the primary (γ-Fe) and the liquid occurs through a peritectic reaction or a direct peritectic solidification. A triple junction (γ-Fe)–(Au)–ℓ can be seen (see letter A in Fig. 6), as well as a subsequent change in contour of the primary phase (B), which may indicate a peritectic reaction. Furthermore, the liquidus lines of (γ-Fe) and (Au) are quite close, which may allow the peritectic reaction to occur [24]. However, this change in contour could also be related to instabilities developing during solid-state transformation following direct peritectic solidification at the (Au)–(γ-Fe) interface. Indeed, very few experimental evidences of peritectic reaction have been documented in literature [18,24].

Once a peritectic layer is formed at the (γ-Fe)–ℓ interface, it grows through direct solidification and/or transformation until all the liquid is fully solidified (C). Considering Figs. 3 and 6, the (Au) phase forms over a solidification interval of only 14 K, whereas the equilibrium solidification interval of (Au) for $X_{Au} = 0.43$ is about 50 K. In can be seen on the phase diagram (Fig. 1) that the solvus and solidus lines of the peritectic phase have slopes of the same sign but of quite different value, indicating that a strong composition gradient takes place in the peritectic phase as the temperature decreases. This gradient, which is associated with the high diffusion coefficient in the (Au) phase [21], promotes the peritectic transformation that occurs by solute diffusion through the peritectic phase [25,26]. Indeed, a one-dimensional diffusion calculation in all three phases and accounting for macrosegregation phenomena gives a value of 12 K [27], quite close to the 14 K measured.

4.4. fcc phase miscibility gap

As mentioned earlier, (γ-Fe) and (Au) are actually the same fcc phase that undergoes a miscibility gap at temperatures lower than 1248 °C (i.e. the maximum of the thick line in Fig. 1). In this miscibility gap, the solubilities of iron

in (Au) and of gold in (γ-Fe) decrease with temperature. The mechanisms by which both phases reduce their supersaturation are now explained.

The first of these mechanisms is an exchange of solute elements near the (Au)–(γ-Fe) interface, leading to particle-free zones (PFZs) on both sides of the interface and precipitates at some distance from it (Fig. 7). Once the peritectic phase has formed ($T_1 \approx 1160\,^{\circ}C$), the composition profile in both phases looks like the one schematically shown at the top of Fig. 7a. As the temperature decreases to T_2 (Fig. 7a, bottom, for $T_2 \approx 1050\,^{\circ}C$), the solubility in each phase has decreased and the two interfacial compositions spread apart. This induces a minimum and maximum in the composition profile of the (Au)-, respectively (γ-Fe)-, phase, at some distance from the interface (dashed vertical lines). When the supersaturation reaches a critical level at these locations, precipitation occurs, draining the solute elements toward the precipitates and leaving a PFZ zone in between.

A microstructure resulting from this mechanism is illustrated in Fig. 7b, with arrows pointing out the precipitation locus. Again, the gray-levels in this image are correlated to the gold composition. Around the precipitates and in the PFZ, the (γ-Fe) matrix is darker and the (Au) matrix lighter than their bulk counterparts, indicating a decrease of their respective supersaturation. In both phases, precipitates are strongly oriented with the same direction as the primary phase dendrites (see Fig. 3) and slightly faceted. This is a clear indication that the peritectic phase (Au) has grown with a specific orientation relationship with respect to the primary phase (γ-Fe), and probably with the same crystallographic orientation as they share the same fcc structure. Unfortunately, this relationship could not be verified by electron backscatter diffraction (EBSD) since the (γ-Fe) phase undergoes an allotropic transformation to (α-Fe) during the quench.

As the temperature keeps decreasing, the driving force for precipitation increases and precipitation then proceeds according to two mechanisms, depending on the composition and the velocity imposed by the Bridgman furnace (see Fig. 8). At low speed (Fig. 8a), precipitation of (γ-Fe) in (Au) is continuous (letter A), while precipitation of (Au) in (γ-Fe) is either continuous (letter B), or discontinuous with an interlamellar spacing on the order of 1 μm (letter C). At higher speed (Fig. 8b), precipitation is discontinuous in both phases, with an interlamellar spacing around 0.3 μm. While (γ-Fe) and (Au) are the same phases that enter into a miscibility gap below the peritectic temperature, their different precipitation behavior can be related to their respective melting points. For discontinuous precipitation to occur, diffusion at the precipitation front, i.e. at grain boundaries, must dominate bulk diffusion. This typically occurs below 0.75–0.8 T_m of each phase [28], thus explaining why, at a given temperature where precipitation occurs ($T_2 \approx 1050\,^{\circ}C$), bulk diffusion in gold is easier than in austenite.

The transition from continuous to discontinuous precipitation is not only influenced by temperature: the cooling rate (i.e. velocity) also plays a role. With an increasing cooling rate, the distances for bulk diffusion decrease and discontinuous precipitation is favored. On the other hand, the microsegregation profiles shown in Fig. 7 also have an

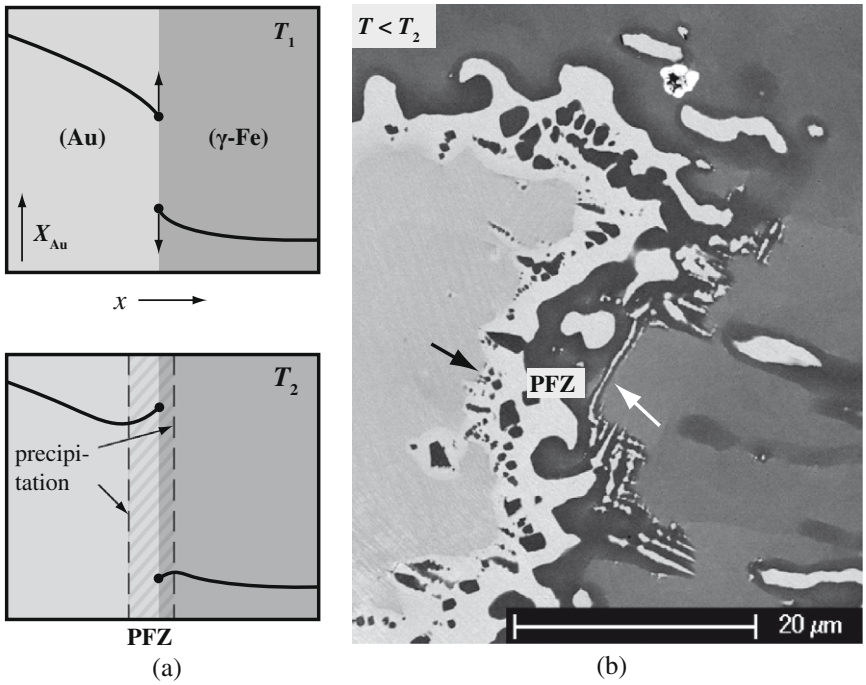

Fig. 7. Diffusion, precipitation and formation of a PFZ near the (Au)–(γ-Fe) interface due to the miscibility gap of the fcc phase. (a) Schematic diagram; (b) resulting microstructure at $T_2 \approx 1050\,^{\circ}C$ (SEM-BSE image).

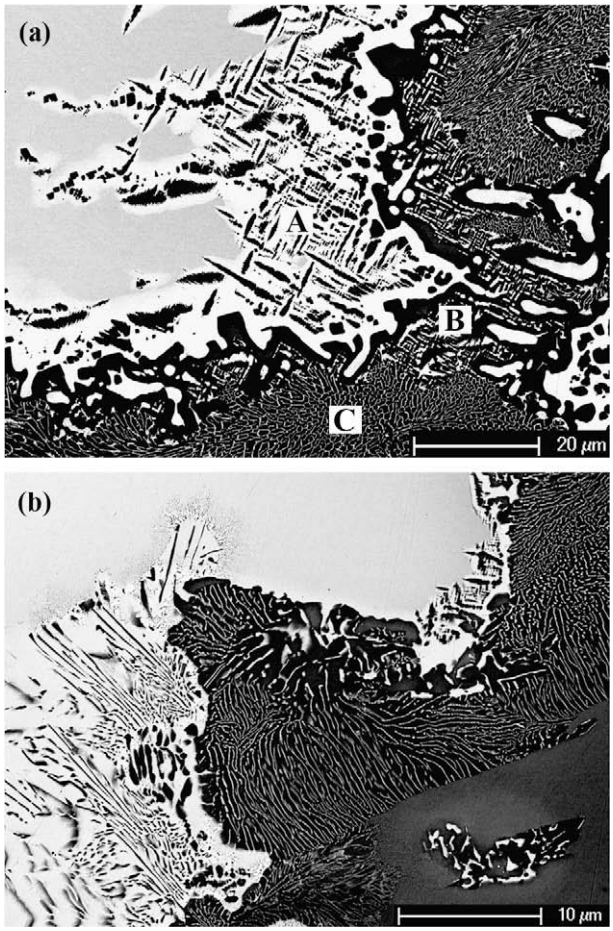

Fig. 8. Precipitation of (Au) in (γ-Fe) and of (γ-Fe) in (Au): (a) $v = 1.67\ \mu m\ s^{-1}$; (b) $v = 33.4\ \mu m\ s^{-1}$.

influence on the precipitation mechanism: the (γ-Fe) phase exhibits a flatter microsegregation profile compared to the (Au) phase [27], thus further reducing bulk diffusion in austenite.

While crystallographic orientation analysis of the (γ-Fe) phase is not possible (see above), an EBSD analysis of the (Au) phase has been conducted. No evident orientation relationship could be found between the supersaturated matrix ahead of the discontinuous precipitation front and the depleted matrix behind it. This crystallographic orientation discontinuity at the precipitation front confirms the nature of the discontinuous precipitation [29].

4.5. Eutectoid reaction and (α-Fe) ferrite precipitation

Below 868° C, primary (γ-Fe) decomposes into (Au) and (α-Fe) through a eutectoid reaction. Since the gold phase is already present in the (γ-Fe) phase via the discontinuous precipitation, this reaction occurs by a slight thickening of the existing gold lamellae and a corresponding gold-impoverishment of the iron phase, which transforms into (α-Fe) (Fig. 3d).

Since the (Au) phase is still supersaturated with iron below the eutectoid temperature, acicular ferrite precipitates also form within this phase (Fig. 3e). As seen in the micrograph of Fig. 9a, three orientations can be identified for these precipitates: (1) parallel to the (γ-Fe) dendrites (24° with respect to the vertical thermal gradient direction *G*); (2) normal to direction (1); (3) with an angle of 30° with respect to direction (1). Precipitates oriented along direction (3) look "blurred", as if they were cut nearly parallel to the section plane.

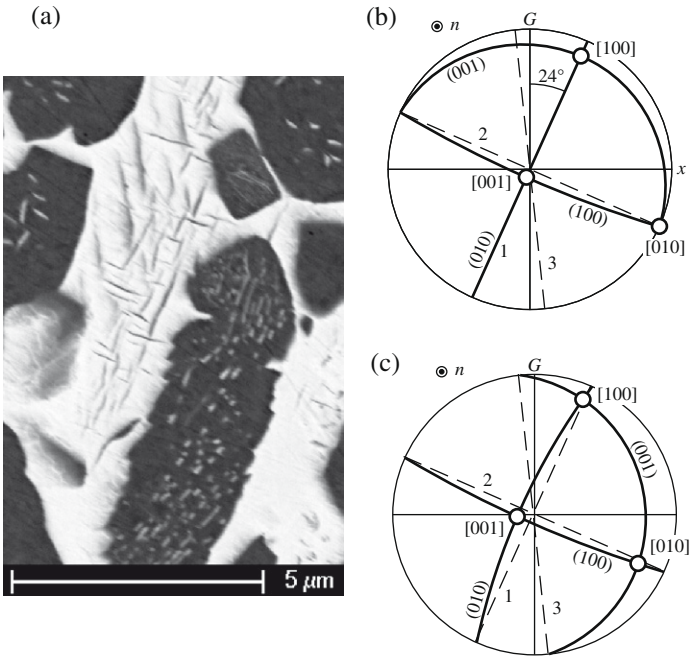

Fig. 9. (a) (α-Fe) Ferrite precipitation in the (Au) phase, viewed in a longitudinal section (here the thermal gradient *G* is vertical) $v = 1.67\ \mu m\ s^{-1}$. (b) $\langle 100 \rangle$ pole figure of the expected orientation of the (Au) matrix, showing the $\{100\}$ plane traces (plain arc of circles) and the acicular ferrite precipitate orientation in this section (dashed lines); (c) same as (b) with a 12° rotation about the [100] axis.

The orientation of these acicular ferrite plates in this section are shown with dashed lines in the stereographic projections shown in Fig. 9b and c, the axes of which are the same as those of the section micrograph in Fig. 9a. Although EBSD measurements could not be conducted on this section, the orientation of the (Au) matrix was assumed to be identical to that of the (γ-Fe) dendrites, the latter being assumed to grow along $\langle 100 \rangle$ directions. As already discussed, the primary trunks of the dendrites in this specimen are growing at 24° from G and 7° from the section plane. This direction is reported in the stereographic projections. Assuming secondary dendrite arms to be in (or perpendicular to) the section plane, the $\langle 100 \rangle$ pole figure of the (Au) matrix is shown in Fig. 9b. As can be seen, the directions (1) and (2) of the (α-Fe) precipitates correspond well to the intersections of the (100) and (010) planes of (Au) with the metallographic section, but the third orientation of the precipitates does not.

However, two factors should be kept in mind: (i) the [100] direction is fairly well defined by the (γ-Fe) dendrite trunk direction, which is not the case for the [010] direction deduced from the secondary arms; (ii) the (001) plane is nearly parallel to the section plane and a small rotation can drastically change their intersection. Indeed, a rotation of 12° about the [100] direction can bring this intersection into coincidence with the third orientation of the precipitates, without changing noticeably the two other orientations (see $\langle 100 \rangle$ pole figure, Fig. 9c).

From these observations, it is concluded that acicular ferrite precipitates in the (Au) phase as {100} platelets in coincidence with {100} planes of (Au). This coincidence relationship also explains the "blurred" appearance of the third type of precipitates, since the (001) plane is nearly parallel to the section plane. Unlike the usual Nishiyama–Wassermann (N–W) or Kurdjumov–Sachs (K–S) orientation relationship between fcc austenite and bcc ferrite, bcc (α-Fe) and fcc (Au) are such that $\{100\}_{\alpha}//\{100\}_{(Au)}$. Such observations are consistent with the relationships proposed by Frebel [9–11] for the (α-Fe) precipitation from (Au), based on the precipitation of (Au) platelets from (α-Fe) [30]: $\{100\}_{\alpha}//\{100\}_{(Au)}$ and $\langle 110 \rangle_{\alpha}//\langle 100 \rangle_{(Au)}$. Concerning the competition between the precipitation between (α-Fe) and (γ-Fe) in (Au) [13], one might argue that these precipitates are in fact (γ-Fe). However, the distinct composition jump observed at the eutectoid temperature for the iron phase (see Fig. 4) as well as the distinct morphology and orientation between these acicular precipitates and the (γ-Fe) ones (see Fig. 8a, letter A) indicate that they are most probably (α-Fe).

5. Conclusions

Solidification and solid-state transformations upon cooling of an Fe–22 at.% Au hypoperitectic alloy have been characterized through DTA and interrupted Bridgman solidification experiments. Similar but complementary observations were made using both techniques:

- During dendritic solidification of the primary (γ-Fe) phase, macrosegregation related to natural convection tends to increase any small curvature of the isotherms. The dendrite front curvature is further increased by shrinkage-induced macrosegregation, since the liquid density can increase due to gold rejection. Dendrite arm coarsening follows a power law with an exponent of 1/3.55.
- The formation of the peritectic (Au) phase occurs over a temperature interval of about 14 K. It is unclear whether nucleation is the result of peritectic reaction or direct solidification. The peritectic phase grows essentially through peritectic transformation.
- Since (Au) and (γ-Fe) are the same fcc phase, they enter a miscibility gap directly below the peritectic temperature: (γ-Fe) precipitates within (Au) and (Au) precipitates within (γ-Fe). In addition to the formation of a PFZ at the interface of the primary and peritectic phases, precipitation progresses in a continuous or discontinuous mode, depending on the parent phase ((Au) or (γ-Fe)) and cooling conditions.
- At the eutectoid temperature, (γ-Fe) transforms into (α-Fe) and (Au), thus slightly increasing the fraction of (Au) phase already present in the iron phase. Below the eutectoid temperature, the (Au) phase is supersaturated and acicular ferrite precipitates with the same coherency relationship previously described for this system [30].

This detailed description of microstructure formation in the Au–Fe system is a fundamental basis for the understanding of the more complex metallurgical phenomena occurring during laser welding of dissimilar 18 carat gold and austenitic stainless steel [16].

Acknowledgement

The authors would like to thank the Center for Electron Microscopy (CIME) of EPFL for the electron microscopy observations.

References

[1] Pinasco MR, Piccardo P, Ricci E, Rosellini C. Prakt Metallogr 2002;39:478.
[2] Santos ML, Acciari HA, Vercik LCO, Guastaldi AC. Mater Lett 2003;57:1888.
[3] Sun Z, Ion JC. J Mater Sci 1995;30:4205.
[4] Okamoto H. Phase diagrams of binary gold alloys. Materials Parks (OH): ASM International; 1993.
[5] Raub E, Walter P. Z Metallkde 1950;41:234.
[6] Köster W, Ulrich W. Z Metallkde 1961;52:383.
[7] Coles BR, Sarkissian BVB, Taylor RH. Philos Mag B 1978;37:489.
[8] Wang JQ, Xiong P, Xiao G. Phys Rev B 1993;47:8341.
[9] Frebel M, Predel B. Z Metallkde 1973;64:913.
[10] Frebel M, Predel B. Archiv Eisenhttenwes 1974;7:483.
[11] Frebel M, Schenk J. Z Metallkde 1979;70:55.
[12] Fratzl P, Langmayr F, Yoshida M. Phys Rev B 1991;44:4192.
[13] Bosco E, Rizzi P, Baricco M. Mater Sci Eng A 2004;375–377:468.

[14] Brown ME. Differential thermal analysis. Introduction to thermal analysis. London: Chapman and Hall; 1988. p. 23.
[15] Vandyoussefi M. PhD thesis, Swiss Federal Institute of Technology, Lausanne, EPFL; 1997.
[16] Favez D. PhD thesis, Swiss Federal Institute of Technology, Lausanne, EPFL; 2009.
[17] Goldstein I. Scanning electron microscopy and X-ray microanalysis. New York: Plenum Press; 1981. p. 76.
[18] Kerr HW, Kurz W. Int Mater Rev 1996;41:129.
[19] Cisse J, Kerr HG, Bolling GF. Metall Trans 1974;5:633.
[20] Brandes EA, Smithells CJ. Smithells metals reference book. 7th ed. Oxford: Butterworth-Heinemann; 1999.
[21] Iijima Y, Yamazaki Y. Defect Diffus Forum 2005;237–240:62.
[22] Burden MH, Hebditch DJ, Hunt JD. J Cryst Growth 1973;20:121.
[23] Kurz W, Fisher DJ. Fundamentals of solidification. 4th ed. Zurich: Trans Tech; 1998. p. 69, 105.
[24] St John DH. Acta Metall Mater 1990;38:631.
[25] St John DH, Hogan LM. Acta Metall 1987;35:171.
[26] Ha HP, Hunt JD. Metall Mater Trans A 2000;31:29.
[27] Favez D, Rappaz M. MCWASP XII, TMS; 2009.
[28] Porter DA, Easterling KE. Phase transformations in metals and alloys. Cheltenham: Stanley Thornes; 2000. p. 98, 317.
[29] Manna I, Pabi SK, Gust W. Int Mater Rev 2001;46:53.
[30] Hornbogen E, Roth M. Archiv Eisenhttenwes 1965;36:201.